Noname manuscript No.
(will be inserted by the editor)

Albedo Observation by Hayabusa2 LIDAR: Instrument Performance and Error Evaluation

Ryuhei Yamada[1] · Hiroki Senshu[2] · Noriyuki Namiki[1] · Takahide Mizuno[3] · Shinsuke Abe[4] · Fumi Yoshida[5] · Hirotomo Noda[1] · Naru Hirata[6] · Shoko Oshigami[1] · Hiroshi Araki[1] · Yoshiaki Ishihara[3] · Koji Matsumoto[1]

Received: date / Accepted: date

Abstract The Japanese asteroid explorer Hayabusa2 was launched at the end of 2014. Hayabusa2 is supposed to observe the near-Earth C-type asteroid 162173 Ryugu (1999 JU3) and bring surface material samples back to Earth in 2020. It is equipped with Light Detection and Ranging (LIDAR) instrument for laser ranging which can be used to measure the intensities of transmitted and received pulses. The intensity data can be used to estimate the normal albedo of Ryugu at a laser wavelength of 1.064 μm. To perform this estimation, we determined the transfer functions of the laser module and receiver to convert the intensity data into pulse energies, along with the utilization ratio of the returned pulse energy, through verification tests of the LIDAR flight model. Then, we evaluated the error of the normal albedo. This error is affected not only by the performance of the LIDAR but also by the slope and roughness of the asteroid's surface. In this paper, we focus on the error in the normal albedo due only to the instrument error, which will be 18.0% in an observation at a nominal altitude of 20 km.

Keywords C-type asteroid· Normal albedo · Laser altimeter· Hayabusa2· Asteroid exploration

[1]National Astronomical Observatory of Japan, RISE Project, 2-21-1, Osawa, Mitaka, Tokyo 181-8588, Japan

Tel.: +81-422-34-3912
Fax: +81-422-34-3596
E-mail: r.yamada@nao.ac.jp

[2]Chiba Institute of Technology, Planetary Exploration Research Center, 2-17-1 Tsudanuma, Narashino, Chiba 275-0016, Japan

[3]Institute of Space and Astronautical Science, Japan Aerospace Exploration Agency, 3-1-1, Yosinodai, Chuo-ku, Sagamihara, Kanagawa 252-5210, Japan

[4]Nihon University, College of Science and Technology, Department of Aerospace Engineering, , 7-24-1, Narashinodai, , Funabashi, Chiba 274-8510, Japan

[5]National Astronomical Observatory of Japan, Office of International Relations, 2-21-1, Osawa, Mitaka, Tokyo 181-8588, Japan

[6]University of Aizu, Research Center for Advanced Information Science and Technology, Aizu-Wakamatsu, Fukushima 965-8580, Japan

1 Introduction

The Japanese asteroid explorer Hayabusa2 was launched in December 2014 to observe the carbonaceous (C-type) asteroid 162173 Ryugu (1999 JU3), which is one of the near-Earth and potentially hazardous asteroids (PHAs). We will observe the surface topography, gravity, thermal state, and albedo of the asteroid using remote-sensing instruments, and the samples collected will be brought back to Earth at the end of 2020. The "albedo" is defined as the reflectance in a specific range of wavelengths, and provides very important information about the composition and state of the asteroid's surface. The albedo is also used to determine the taxonomic type of asteroid. The majority of C-type asteroids are located in the outer main belt, and they typically have low albedos. We have less information about the albedos of C-type asteroids and their variation than S-type asteroids.

There are three possible causes for albedo variation on the surface of a C-type asteroid. First, albedo variation may indicate a degree of space weathering. PHAs such as Ryugu have likely experienced frequent close encounters with the Earth. Because of the planetary tidal effects of these close encounters, the asteroid may have been resurfaced as a result of the sliding of its surface regolith (Binzel et al., 2010). Both tidal effects and particle bombardment could have exposed fresh, non-weathered material on the surface of the asteroid. Second, the albedo variation may be an evidence of aqueous alternation. One of the optical spectra of Ryugu indicates absorption at around 0.7 μm, which is related to aqueous alteration (Vilas, 2008). However, this absorption disappeared in the spectra taken on different dates (Moskovitz et al., 2013, Sugita et al., 2013). Third, the material delivered from other bodies as a result of impacts could also cause the albedo variation, as seen in the dark rays on 4 Vesta (Reddy et al., 2012), and maybe in black boulders on 25143 Itokawa (Hirata and Ishiguro, 2011) .

In spite of these possibilities, we could not definitively find albedo variations on the body. The first and only close-up observation of a C-type asteroid was performed for 253 Mathilde, a main belt asteroid, through a fly-by of NASA's asteroid explorer NEAR Shoemaker in June 1997 (Ververka et al., 1997). The measurement using the multi-spectral imager onboard NEAR revealed that the geometric albedo of Mathilde was 0.047 ± 0.005 at a wavelength of 0.55 μm, and the variation on the surface was within ±6% of the mean (Clark et al., 1999). These values are consistent with the range for C-type asteroids (0.03 - 0.06 (Tedesco, 1992)). We could not find evidence of albedo variation on Mathilde. However, the closest approach to Mathilde was at a large distance of about 1200 km and lasted only 40 min, which allowed a limited area to be imaged at a resolution of about 500 m per pixel (Ververka et al., 1997). The data were probably insufficient to identify an albedo variation. In the Hayabusa2 mission, the albedo will be measured at an altitude of 20 km over a year and a half, and we will obtain sufficient data to find a possible albedo variation, such from space weathering and aqueous alternation on Ryugu.

The Hayabusa2 spacecraft has four remote-sensing instruments: optical navigation camera (ONC), near infrared spectrometer 3 (NIRS3), thermal infrared imager (TIR), and laser altimeter (light detection and ranging: LIDAR). In this study, we will use the LIDAR laser altimeter (Fig. 1) to measure the distribution of the normal albedo of Ryugu at a laser wavelength of 1.064 μm based on the intensity data. The main purpose of the LIDAR is to measure the distance between the spacecraft and the asteroid using the time delay between the transmission and reception of the laser. In addition, the Hayabusa2 LIDAR has the function of measuring the intensities of a transmitted laser pulse and received pulse reflected from the surface. We have the advantage of using the laser altimeter to investigate the albedo, compared with three other remote sensing instruments installed on Hayabusa2. The normal albedo estimated from the LIDAR data does not depend on the solar incidence angle because it is measured at a constant zero phase angle, and no photometric normalization is required. As described in Mizuno et al. (2016), the LIDAR has two types of telescopes: 'Near system' and 'Far system' to measure altitudes below and above about 1 km, respectively. Because the normal albedo will be calculated from the measurements using the Far telescope, we only consider this telescope in this paper. The actual characteristics of the LIDAR are summarized in Table. 1.

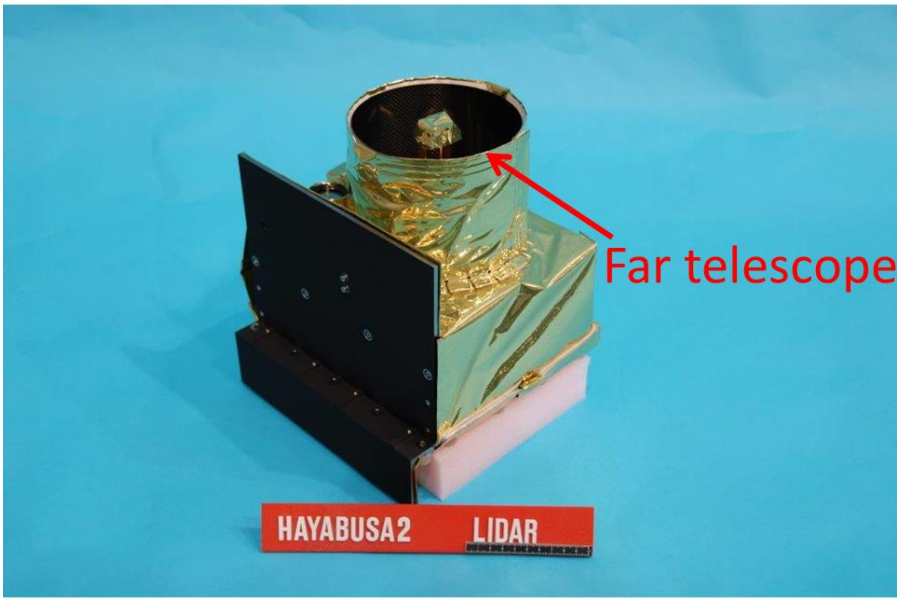

Fig. 1 Photograph of LIDAR flight model

The normal albedo at 1.064 μm has been measured by laser altimeters in some planetary explorations, including the lunar orbit laser altimeter (LOLA) onboard the Lunar Reconnaissance Orbiter (Smith et al., 2010), the Mercury laser altimeter (MLA) onboard the MESSENGER (Cavanaugh et al., 2007, Sun et al., 2015) and the former LIDAR onboard the first Hayabusa (Mukai et al., 2007). The albedo variations found in the LOLA and MLA data are important for geological and geochemical investigations of the surface of the Moon and Mercury, respectively (e.g., Zuber et al., 2012, Neumann et al., 2013, Lucey et al., 2014). On the other hand, the normal albedo of Itokawa has a large amount of ambiguity because the former LIDAR could not simultaneously measure the intensities of the transmitted and received pulses (Abe et al., 2006, Mukai et al., 2007). The Hayabusa2 LIDAR is designed to determine both intensities at every shot (Mizuno et al., 2016).

In this paper, we describe the method used to estimate the normal albedo and evaluate the error using the LIDAR data. This consideration can also be used to plan the operation of Hayabusa2 during the mission phase. The normal albedo is defined as the ratio of the energies of the pulses before and after reflection at the asteroid's surface. The intensities of the transmitted and received laser pulses are recorded by the LIDAR as digital power values. Therefore, the transfer functions of the laser module and receiver have to be determined to convert these digital values into the pulse energies. Then, the reflected pulse energy is estimated considering the ratio of energy input to the field of view of the telescope and the geometric attenuation along the return path. The surface slope and roughness elongate the time width of the returned pulse and decrease the intensity. In this paper, we specially investigate the characteristics of the LIDAR required to estimate the normal albedo and error budgets related to the instrument performance.

Section 2 describes the method used to derive the normal albedo from the LIDAR data and evaluate the error. Section 3 describes experiments using the LIDAR flight model to investigate the transfer functions used to convert the intensity data into the laser energy. Then, in section 4, we quantitatively evaluate the contribution of the instrument error to the normal albedo uncertainty. Finally, section 5 discusses the effects of the slope and roughness of the asteroid's surface.

Table 1 Actual characteristics of Hayabusa2 LIDAR flight model. The column "Descriptions" shows the section where the parameter is evaluated in our measurement.

Parameters	Symbols in the text	Values	Descriptions
Ranging range		30m – 25km (Near system: below 1km Far system: above 1km)	
Transmitted laser pulse energy	E_T	14.6±1.1 mJ	Section 3-1
Wavelength		1.064 μm	
Pulth width	σ_0	$(5.6\pm0.27)\times10^{-9}$ s	Section 3-2
View angle of Far telescope		1.5 mrad	
Full beam divergence of the transmitter	θ_T	2.5 mrad	
Area for laser receiving of the Far telescope	A_0	0.0095 m^2	
Transmissivity of the optical system	β	0.678	
Utilization ratio	ε	0.409±0.017	Section 3-3
Responsivity of the APD for low level	G^L	50±4.5 kV/W	Section 3-2
Responsivity of the APD for middle level	G^M	166±28 kV/W	Section 3-2
Responsivity of the APD for high level	G^H	503±83 kV/W	Section 3-2
Analogue bandwidth of the APD		100 MHz	
Maximum data sampling		1.0 Hz	

2 Calculation of normal albedo

The normal albedo ρ derived from the LIDAR data can be defined as follows:

$$\rho = E_S/E_T \quad (1)$$

where E_T is the energy of a laser pulse transmitted from the LIDAR (Table 1), and E_S is the energy of a pulse reflected from the asteroid surface.

Figure 2 shows a schematic view of the laser module of the LIDAR. In the laser module, a laser pulse is irradiated from a passive Q-switched Nd:YAG with a laser diode (LD) at 1.064 μm. A laser pulse is divided by the mirror, and a small portion of the energy is measured by a pin-photo diode. The remaining energy, E_T, is transmitted to the asteroid surface. The voltage signal from the pin-photo diode is processed through an electrical circuit and recorded as an 8-bit digital value. This is the transmitted pulse

intensity D_T. Because we only obtain D_T during the operation of Hayabusa2, we have to determine the functional relationship between E_T and D_T: $E_T(D_T)$.

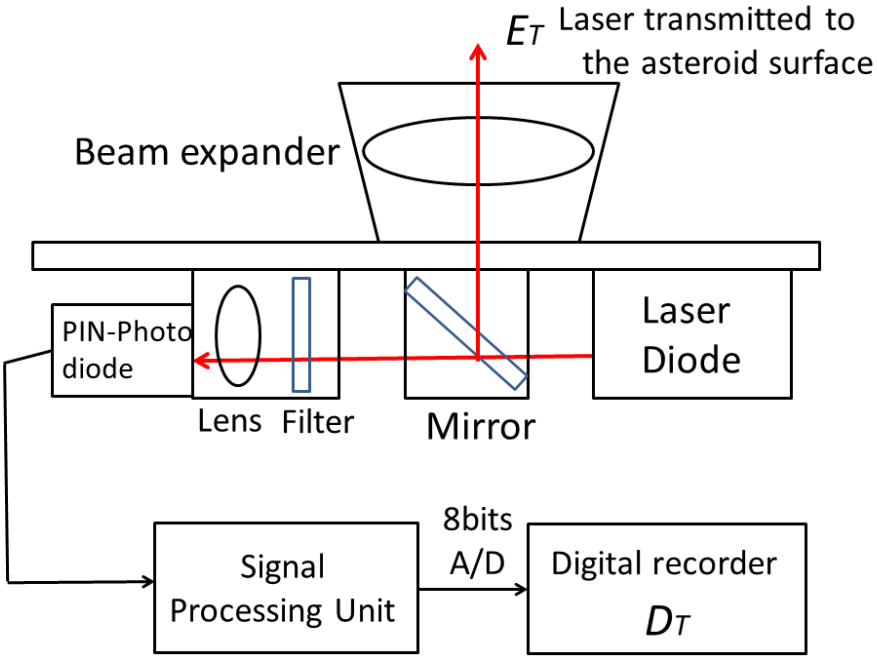

Fig. 2 Schematic view of LIDAR laser module. The red and black arrows show the traveling directions of a transmitted laser pulse and an electrical signal, respectively.

With the assumption of Lambertian reflectance, the energy of the pulse received at the telescope, E_R, can be represented as follows:

$$E_R = \varepsilon E_S \frac{A_0}{\pi L^2} S(\theta_S, \Delta\xi) \quad (2)$$

where L is the distance between the asteroid and the spacecraft, A_0 is the area of the telescope (Table 1), and ε is the utilization ratio of the laser energy. The utilization ratio is the ratio of energy transmitted into the field of view of the telescope compared to the total laser energy. $S(\theta_S, \Delta\xi)$ represents the effects of the surface slope and roughness on the reflected pulse, where θ_S is the inclination of the surface slope, and $\Delta\xi$ is the surface roughness. Because the scope of this paper is an evaluation of the instrument performance, the errors related to $S(\theta_S, \Delta\xi)$ are not taken into account.

The power of the received pulse is measured using an avalanche photodiode (APD). Figure 3 shows a schematic view of the receiver system. The voltage signal from the APD is processed through the amplifier, integration circuit and peak-hold circuit (signal-processing unit), and is recorded as an 8-bit value representing the received pulse intensity D_R. Thus, the E_R is estimated using the transfer function T_R from D_R and transmissivity of the receiver optical system, β (Table 1):

$$E_R = \frac{T_R(D_R)}{\beta}. \quad (3)$$

Then, using Eqs. (2) and (3), E_S can be estimated from D_R as follows:

$$E_S = \frac{\pi L^2}{\varepsilon \beta A_0} T_R(D_R) \frac{1}{S(\theta_R, \Delta\xi)}. \quad (4)$$

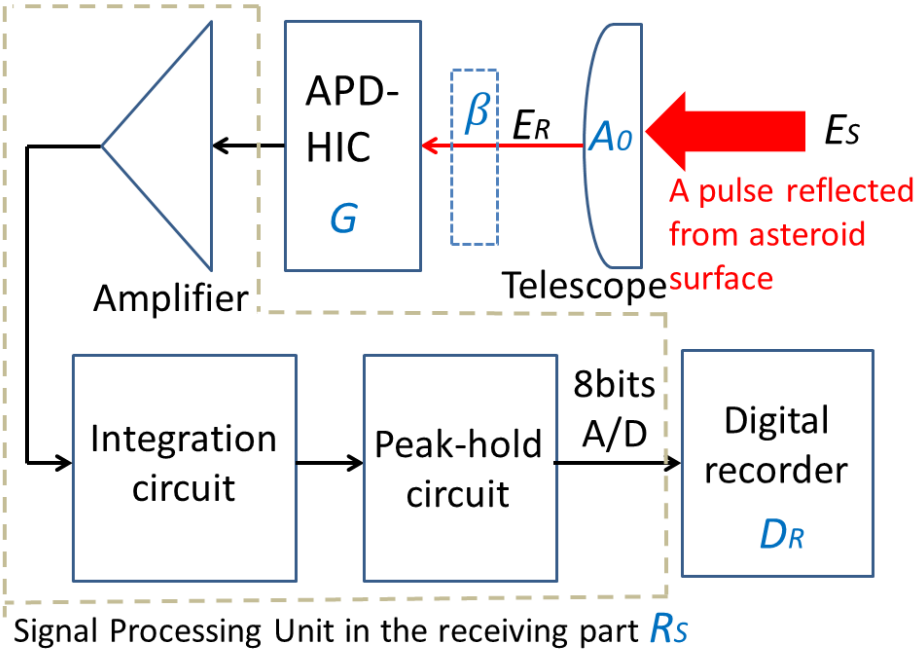

Fig. 3 Schematic view of LIDAR receiver system. The red and black arrows show the travelling directions of a received laser pulse and an electrical signal, respectively.

Finally, we can derive the normal albedo using Eqs. (1) and (4):

$$\rho = \frac{\pi L^2}{\varepsilon \beta A_0} \frac{T_R(D_R)}{E_T(D_T)} \frac{1}{S(\theta_R, \Delta\xi)}. \quad (5)$$

In the above equation, D_T and D_R are obtained as telemetry data from the LIDAR. The distance L can be determined from the ranging data measured by the LIDAR, and we can determine the value with an error of less than 0.1 % above an altitude of about 1 km (Mizuno et al., 2016). Because β and A_0 are precisely known, and $S(\theta_S, \Delta\xi)$ is not taken into account, the errors of $E_T(D_T)$, $T_R(D_R)$, and ε determine that of the normal albedo because of the LIDAR performance, $\delta\rho_I$:

$$\delta\rho_I = \rho \sqrt{\left(\frac{\delta E_T(D_T)}{E_T(D_T)}\right)^2 + \left(\frac{\delta T_R(D_R)}{T_R(D_R)}\right)^2 + \left(\frac{\delta\varepsilon}{\varepsilon}\right)^2}. \quad (6)$$

where $\delta E_T(D_T)$, $\delta T_R(D_R)$, and $\delta\varepsilon$ are the errors of $E_T(D_T)$, $T_R(D_R)$, and ε, respectively.

3 Investigation of LIDAR performance

To evaluate Eqs. (5) and (6) quantitatively, the transfer functions, $E_T(D_T)$, $T_R(D_R)$, and ε of the LIDAR flight model were investigated using verification tests.

3-1. Transfer function of laser module

In order to evaluate $E_T(D_T)$, we measured the transmitted pulse energy E_T and intensity D_T simultaneously. The LIDAR flight model was placed under vacuum and two extreme temperature environments: "cold" and "hot". The "cold" and "hot" environments were defined as the lowest and highest temperatures during the global mapping at an altitude of about 20 km corresponding to the

aphelion and perihelion of the asteroid orbit. We investigated the performance only under these temperature environments because the normal albedo will be mainly measured at the altitude. In this test, the interface temperature between the LIDAR and spacecraft was -20 ℃ in the "cold" environment, and the highest temperature was +12 ℃ in the "hot".

After the temperature of the flight model became stable, E_T and D_T were measured at every second for 30 min in the "hot" and "cold" environments, respectively. In Fig. 4, the "cold" and "hot" data are shown by solid squares and open circles, respectively. As shown in this figure, E_T does not depend on the temperature. It is also clearly demonstrated that E_T is proportional to D_T. Thus, the transfer function is represented by

$$E_T(D_T) = (2.20 \times 10^{-4})D_T - 0.0129 \quad (7).$$

Then, the error of $E_T(D_T)$, $\delta E_T(D_T)$, is evaluated by

$$\delta E_T(D_T) = \sqrt{\frac{\sum_i^N \left(E_T^i - E_T(D_T)_i\right)^2}{N-1}} \quad (8)$$

where E_T^i is the i-th measured transmitted pulse energy value, $E_T(D_T)_i$ is the energy calculated from the i-th D_T using Eq. (7), and N is the number of measured data points. From Eq. (8), E_T can be estimated with an error of 2.5 % over the entire temperature range expected during operation.

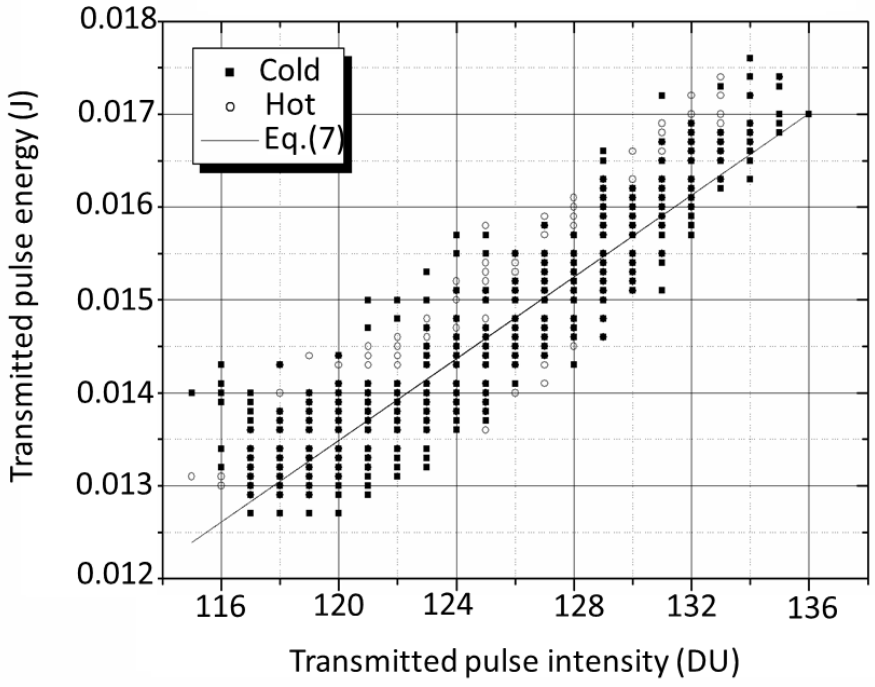

Fig. 4 Relation between transmitted pulse energy and intensity. The Eq. (7) results are also shown by the solid line.

The aging of the laser module was tested in the laboratory. After sixteen million shots, it was verified that the transmitted pulse energy did not change significantly. The total number of shots was more than twice that expected during the operation of the LIDAR. The radiation tolerance of the PIN-PD was also secured by the protection provided by the thick shield of the LIDAR's cover.

3-2. Transfer function of receiver

$T_R(D_R)$ corresponds to the energy input to the APD, and it can be split into three parts: the response of the signal processing unit of the receiver, R_S; the responsivity of the APD, G (Fig. 3), and the received pulse width σ_R. $R_S(D_R)$ gives the peak voltage of the APD output pulse, and G gives the ratio between the peak voltage and the power input into the APD. We can estimate the energy by multiplying σ_R by the power. Therefore, $T_R(D_R)$ is calculated as follows:

$$T_R(D_R) = R_S(D_R)\sigma_R/G. \quad (9)$$

We study $R_S(D_R)$, G, and σ_R in detail below.

First, we investigate $R_S(D_R)$. Rectangular pulses with a constant width of 10 ns were input electrically to the signal processing unit, which changed the peak voltage, and D_R was recorded for each pulse. $R_S(D_R)$ will vary with σ_R, depending on the asteroid surface. However, σ_R was set to be constant in the verification tests. An effect of variable pulse width is discussed later. Figure 5 shows the experimental results. From these results, we found that $R_S(D_R)$ is a nonlinear function of D_R. In Fig. 5, the measurements performed at different temperatures, -10 ℃, +20℃, +25 ℃, and +45 ℃, suggest that $R_S(D_R)$ does not depend on the temperature. Then, the peak voltage of the output pulse from the APD can be estimated using the fourth-order polynomial equation

$$R_S(D_R) = -6.79 \times 10^{-11} D_R^4 + 1.10 \times 10^{-7} D_R^3 - 5.40 \times 10^{-6} D_R^2 + 1.36 \times 10^{-3} D_R + 0.0292 \quad (10)$$

where $R_S(D_R)$ and D_R are in V and DU, respectively.

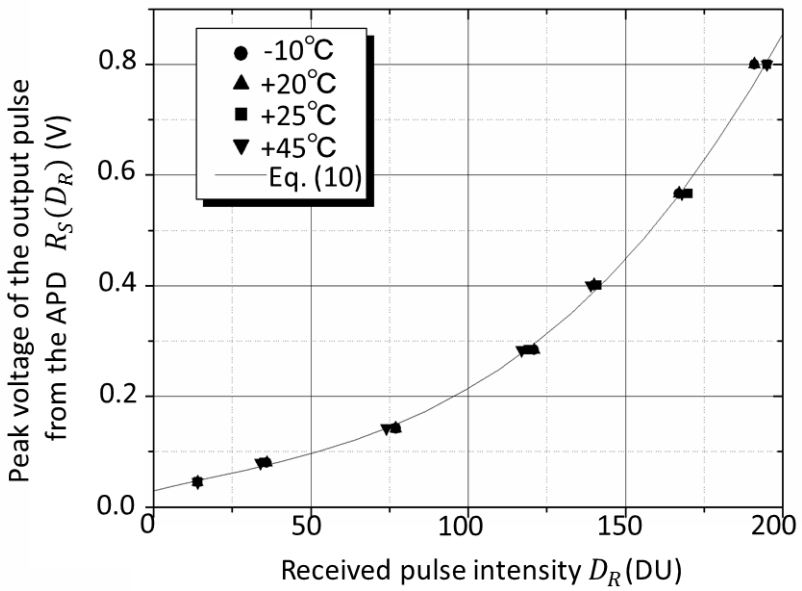

Fig. 5 Response of signal processing unit in receiver. The data measured at four temperatures are shown by circles, triangles, squares and inverse triangles, and the results of Eq. (10) are shown by a solid line.

We evaluated the standard error of $R_S(D_R)$ using the following equation

$$\delta R_S(D_R) = \sqrt{\frac{\sum_i^N \left(V_i^{in} - R_S(D_R)_i\right)^2}{N-1}} \quad (11)$$

where V_i^{in} is the i-th peak voltage of the APD output pulse, and $R_S(D_R)_i$ is the voltage calculated from the i-th D_R using Eq. (10). Then, $\delta R_S(D_R)$ is determined to be 0.011 (V).

Second, we describe the APD's responsivity, G, which changes with the voltage applied to the APD. For albedo measurements, we use three levels of responsivity: low, middle, and high. In our investigation, laser pulses from the PIN-PD with a wavelength and width of 1.064 μm and about 10 ns, respectively, were input into the Far telescope at room temperature, and the D_R values were simultaneously recorded for each pulse. Because the input pulses diverged and scattered in our test configuration, it was difficult to control the power at the desired level. Therefore, we were forced to use the design value for the low responsivity, 50 kV/W (Table 1), as the reference. Then, the relative increases in the middle and high responsivities were evaluated with respect to the low responsivity under the same test configuration. From Eqs. (3) and (9), we can derive

$$\frac{E_R\beta}{\sigma_R} = R_S(D_R)/G \qquad (12)$$

where the left hand side is the laser power input to the APD. When that input power is the same for each responsivity of the APD, the middle and high responsivities, G^M and G^H, are estimated as follows:

$$G^M = G^L\{R_S(D_R^M)/R_S(D_R^L)\} \qquad (13)$$

$$G^H = G^L\{R_S(D_R^H)/R_S(D_R^L)\} \qquad (14)$$

where G^L is the low responsivity of the APD, and D_R^L, D_R^M, and D_R^H are the received pulse intensities for the low, middle and high cases, respectively.

The D_R^L values were measured for about 60 s using two types of filters whose transmissions were15.3 % and 24.7 %. The D_R^M and D_R^H values were also recorded using the same filters for comparison with D_R^L and an 8.8 % filter for a comparison between G^M and G^H. The experimental conditions and results of the measurements are summarized in Table 2. Using D_R^L, D_R^M, D_R^H, and Eqs. (10), (13), and (14), we can derive the middle and high responsivities of the APD. G^M is 166± 28 kV/W, and G^H is 503±83 kV/W. These errors are evaluated using the error of G^L and $\delta R_S(D_R)$, as shown in Eq. (11). It is possible that the responsivity of the APD could be dependent on temperature. However, such a temperature variation is automatically compensated by adjusting the applied voltage. The error in G^L, as well as in G^M and G^H, through the compensation is 5.0%. The error of G^L is calculated from the dispersion of the measurements and ambiguity of the thermal compensation, and is 9.0%.

Table 2 Experimental results for three-types of responsivities: low, middle, and high. The averages of the received pulse intensities were derived from the measurements during 60 s for each filter.

Gains	Transmissivity of Filter	Average of received pulse intensity	Relative sensitivity of APD for low gain
	Non	139±6	
	24.70%	55±5	
Low	15.30%	30±2	1.0
	24.70%	129±6	
	15.30%	106±5	
Middle	8.78%	60±7	3.3±0.6
High	24.70%	222±10	10±1.7

15.30%	177±10
8.78%	123±5

Proton irradiation may influence the responsivity of the APD during the cruising and operation phases. However, the same type of the APD was applied to the laser altimeter (LALT) onboard the Japanese lunar explorer SELENE (Araki et al., 2013) and no APD degradation was identified throughout the two-year observation period.

Finally, we focus on the width of the received pulse. This evaluation is required for the conversion from the laser power to the energy, E_R. In the verification tests, the waveforms of the transmitted pulses were measured by a photoelectric tube in "cold" and "hot" environments. Figure 6 shows an example of the measured pulse. The transmitted pulse width, averaged for both environments, is

$$\sigma_0 = (5.64 \pm 0.27) \times 10^{-9} \quad \text{(s)}. \tag{15}$$

The pulse width is defined as half the bandwidth. We found that the width did not differ significantly across the possible temperature range.

When the transmitted laser is reflected at the asteroid surface, the pulse width can elongate as a result of the surface slope and roughness. σ_R would be longer than σ_0, and σ_R has to be estimated using σ_0 and the surface information. We discuss this further in section 5. Here, we assume that the error of σ_R is the same as that of σ_0, that is 4.8%. Then, the $\delta T_R(D_R)$ values for G^L, G^M, and G^H are evaluated using the errors of G, σ_R, and $\delta R_S(D_R)$, and found to be 15.0%, 19.0%, and 17.3%, respectively.

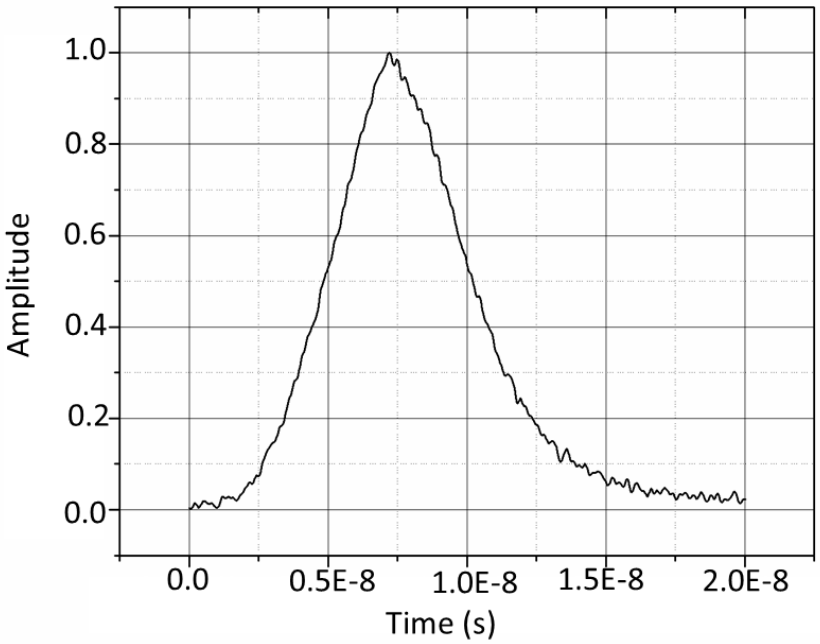

Fig. 6 Example of transmitted laser pulse waveform. The amplitude is normalized to the peak value of the pulse.

3-3. Utilization ratio of laser energy

We have imaged the transmitted laser beam and field of view of the Far telescope using a two-

dimensional CCD sensor. These images were taken in a thermal vacuum test (section 3-1). Figure 7 shows an example of the projected energy distribution of a transmitted laser pulse. The field of view is also indicated by a green line. This figure shows that the far beam pattern is uneven, and the energy spreads outside of the field of view. For this reason, any misalignment between the axis of the transmitting laser and the telescope significantly affects the utilization ratio.

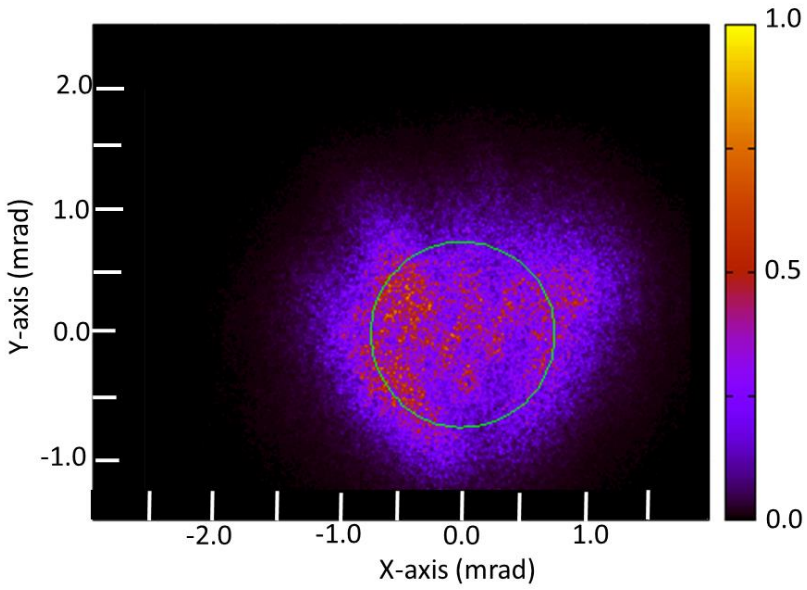

Fig. 7 Far beam pattern of transmitted laser pulse. The green circle indicates the field of view of the Far telescope (1.5 mrad), and the origin is the center of the field of view. The relative strength of the energy is shown by the color, where a brighter color indicates stronger energy.

The value of ε is derived from the ratio of the energy within the field of view to the total energy in the image. We investigated the values of ε in the "cold" and "hot" environments. Figure 8 shows the utilization ratio measured in these two environments during 10 min with a sampling frequency of 1 Hz. The averages of the utilization ratios in each environment are

$$\varepsilon^C = 0.415 \pm 0.014$$
$$\varepsilon^H = 0.403 \pm 0.017. \quad (16)$$

Because the two values in Eq. (16) are indistinguishable, we adopt a single value for the utilization ratio as the average of all the data, that is

$$\varepsilon = 0.409 \pm 0.017. \quad (17)$$

Thus, we can estimate the ratio of the energy input within the field of view of the Far telescope with an error of about 4.2 %. The error of ε includes the thermal variation of the alignment and fluctuation of the far beam pattern. The short-term variations of ε shown in Fig. 8 are probably mainly due to the beam fluctuations. Vibration at the time of the launch may have caused an additional misalignment between the axis of the transmitting laser beam and the field of view. Based on a vibration test before the launch, a misalignment at the launch was likely to occur along the X-axis and to be less than 0.2 mrad. Such a small misalignment is within the error in Eq. (17). The measured characteristics and errors in this section are summarized in Table 1.

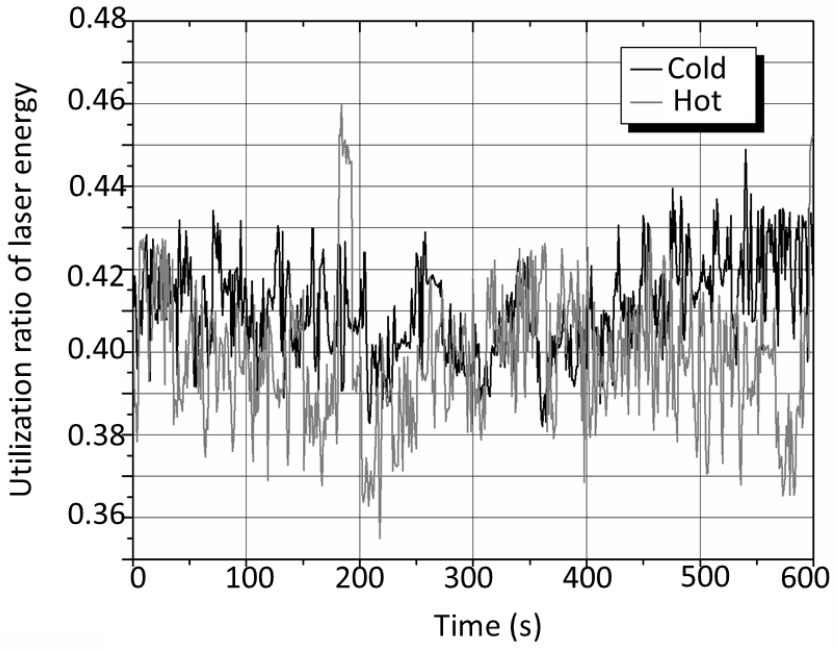

Fig. 8 Utilization ratio of laser energy during 600 s under "cold" and "hot" environments. The outliers at approximately 200 s in the "hot" environment are caused by the rapid fluctuation of the transmitted laser beam pattern.

4 Error in the normal albedo with spacecraft altitude

In this section, we evaluate $\delta\rho_I$ in relation to L. Assuming that the asteroid surface is flat ($\sigma_R = \sigma_0, S = 1$), the expected received pulse intensity D_R' can be calculated for different altitudes:

$$D_R' = \rho \frac{\varepsilon G \beta A_0}{\pi L^2 \sigma_R} \frac{E_T}{R_S} \tag{18}$$

In Eq. (18), the measured values of ε, G, σ_0, and E_T listed in Table 1 are used. During operations of the LIDAR, the APD's responsivity is automatically switched between high and low depending on D_R and L. At an altitude of about 20 km, the high responsivity is selected. During descent to Ryugu, when D_R is over 249, the responsivity changes to the low mode to avoid saturation. The G^Lor G^H listed in Table 1 are applied following the switching condition. In actual operation, the responsivity can also be changed manually, and the middle responsivity can be used.

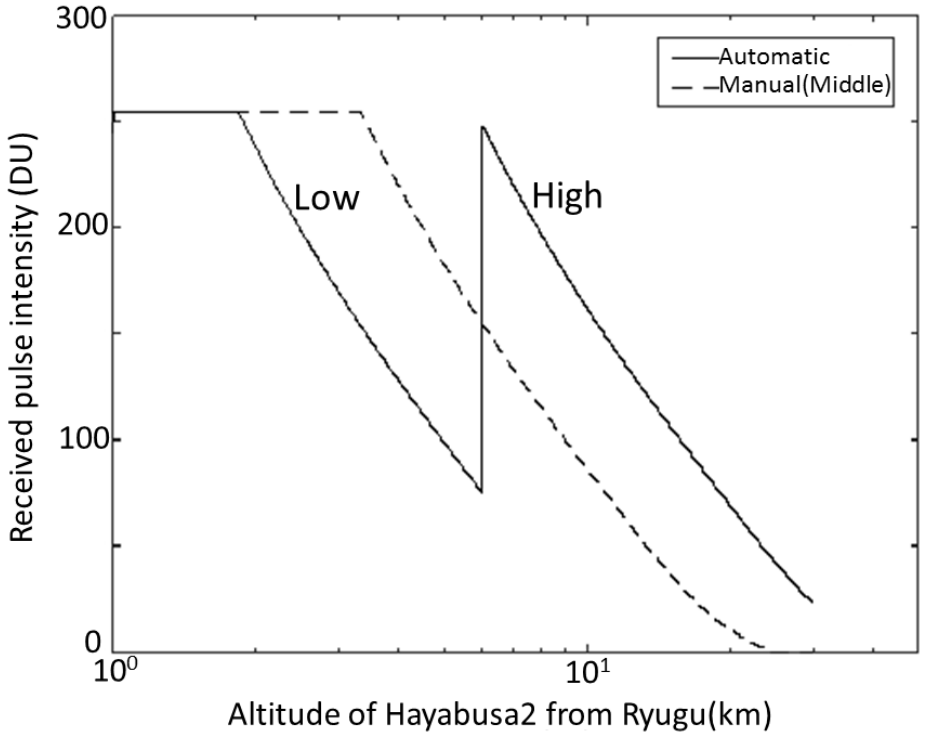

Fig. 9 Simulated received pulse intensity with altitude of Hayabusa2 on assumption of flat surface in the Far telescope range. In this profile, the solid line shows the D_R' observed by the high and low responsivities, which are switched automatically depending on the altitude and D_R'. The expected intensity for the middle responsivity selected manually is shown by the dashed line.

The D_R' calculated from Eq. (18) is shown in Fig. 9. In this calculation, we assume that ρ is 0.047 ± 0.003 based on the geometric albedo determined by a recent ground observation of Ryugu (Ishiguro et al., 2014). It should be noted that, in Fig. 9, we assume a flat surface, for which the opposition effect enhances the reflection intensity. Thus, the calculated values in Fig. 9 show the upper bound of D_R'. This figure shows, that we can measure D_R' without saturation in a range of approximately 2-6 km using the low responsivity and over about 6 km using the high responsivity in the Far system. D_R' could be also measured by the Far system from about 3 to 20 km using the middle responsivity. For altitudes higher than 2 km, D_R' is anticipated not to saturate. Therefore, in this range, $\delta\rho_I$ can be estimated from Eq. (6). $\delta\rho_I$ is 15.8% in the low responsivity range and 18.0% in the high range. These values can be significantly improved by multiple observations of the same surface spot.

5 Discussions

We estimated the instrument's influence on the normal albedo to be an error of 18.0% in the observation from the home position (an altitude of 20 km). Based on the results of the experimental studies, space weathering on a C-type asteroid could change the albedo by more than 30 % at 1.064 μm (Matsuoka et al., 2015), and aqueous alteration could also cause a variation of more than 40 % (Cloutis et al., 2012). In the case of the S-type asteroid Itokawa, an albedo variation of 15-30 % were found in images taken by an optical camera (e.g., Saito et al., 2006). Such variations on Ryugu can be detected from the LIDAR data after the effects of the surface slope and roughness are accurately removed.

If the surface is inclined, the travel time of the pulse reflected from the highest feature found within the laser footprint will be shorter than that from the lowest. Then, the pulse width will elongate depending on the inclination of the slope and altitude of Hayabusa2 as the laser footprint size increases with the

altitude. The analog bandwidth of the APD (Table 1) is narrow enough to allow a reflected pulse longer than σ_0 to also be treated. However, the peak hold circuit in the signal processing unit shown in Fig. 3 has capacitances. Therefore, for the elongated return, D_R may vary depending on the time constant even if the albedo of the reflected surface is the same. In addition, the area of the received pulse can change as a result of multiple reflections and the shadowing caused by the roughness within the laser footprint (e.g., Cord et al., 2003).

Here, we describe how a reflected pulse is deformed as a result of the slope and roughness. The variation of the pulse width caused by the surface slope and roughness is calculated by

$$\sigma_R = \sqrt{\sigma_0^2 + \left(\frac{2Ltan\theta_T tan\theta_S}{c}\right)^2 + \left(\frac{2\Delta\xi}{c}\right)^2} \quad (19)$$

where c is the speed of light, θ_T is the beam divergence of the transmitter (Table1) (Santovito et al., 2006). Figure 10 shows σ_R as a function of the inclination given a constant surface roughness of 1 m at several altitudes. Based on ground observations, Ryugu is likely to have an ellipsoidal body. The largest inclination angle between a normal vector on the ellipsoidal body and a line from the gravity center to the spacecraft may be less than approximately 15°. Thus, the pulse width could be elongated to about 80 ns at the altitude of 20 km, as shown in Fig. 10.

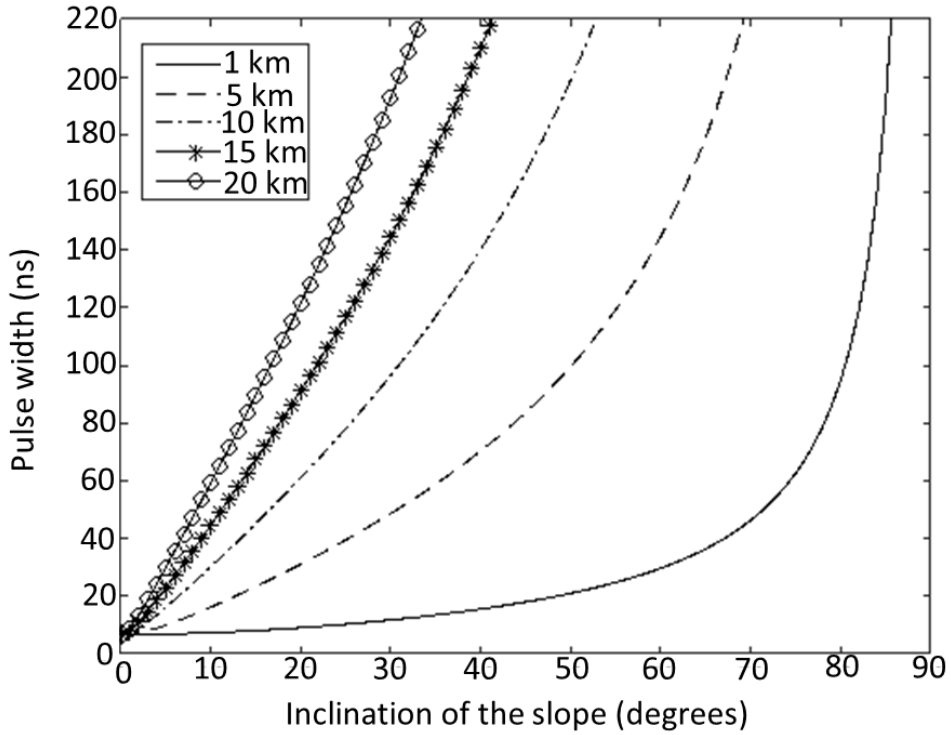

Fig. 10 Pulse width as function of inclination of slope with roughness of 1 m. The widths are calculated at five altitudes; 1, 5, 10, 15 and 20 km.

We have developed code to simulate the deformation of a reflected pulse waveform due to the surface topography. In this calculation, a laser footprint is divided into small elements. For a given topography, the return from each element is integrated into a reflected pulse (e.g., Lohani et al., 2008). On Itokawa, highland areas with a roughness of 2-4 m were found (Barnouin-Jha et al., 2008). In order to simulate the waveform reflected from such a rough terrain, we calculate a pulse reflected from parallel linear hills with a height of 5 m and width of 10 m as an example. We assume that the altitude of the spacecraft is 20 km and that the transmitted pulse has a Gaussian shape in space and time, with a width of 10 ns. The calculated waveform is shown in Fig. 11 by a solid line. A dashed line also shows the reflection from a

flat and smooth surface. This figure shows that the peak level of the reflected pulse is lowered by one order of magnitude, and the width elongates to about 80 ns. This calculation is applicable to simulate a pulse reflected from Ryugu and correct for the effects of the surface using the actual topographic data.

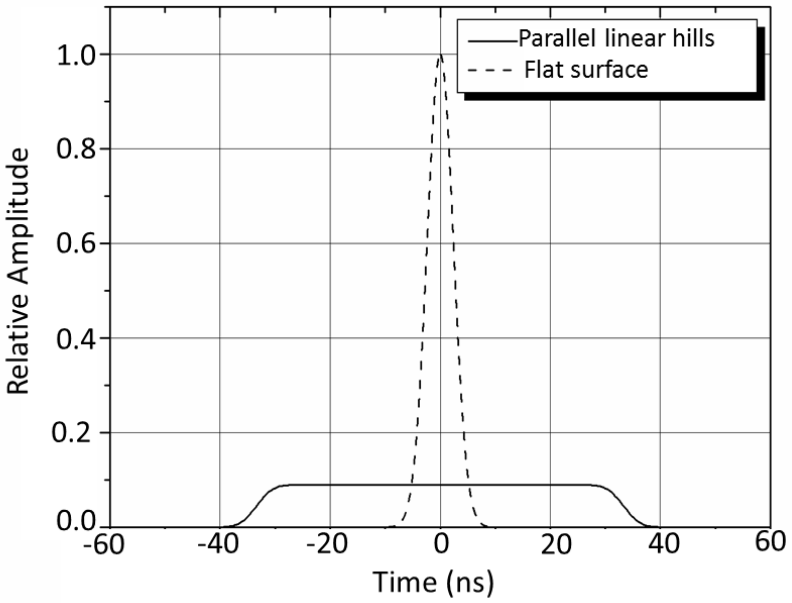

Fig. 11 Comparison between pulse waveform reflected from parallel linear hills with scale of 5 m and that from flat surface. The laser pulse, which has a Gaussian shape in space and time, is shot at an altitude of 20 km. The amplitude is normalized to the peak value of the pulse reflected from the flat surface.

The actual topography will be investigated based on the shape model of the asteroid constructed from LIDAR ranging data and photographs taken by the optical camera (e.g., Namiki et al., 2014). Gaskell et al., (2006) showed that the shape model of Itokawa could be constructed with an error of 0.16 m using images taken from an altitude of 7 km. Although the spatial resolution of the images of Ryugu taken at the nominal altitude (20 km) will be lower than that for Itokawa, Hayabusa2 plans to obtain more close-up images from an altitude lower than 5 km. Therefore, the resolution of the Ryugu shape model will likely have sufficient accuracy to simulate a reflected pulse. In addition, the roughness can be estimated from close images taken by the thermal infrared imager. If we can calculate a reflected pulse using these complementary data sets, the effect of the slope and roughness can be adequately removed from each D_R. For this purpose, we need to investigate the alignment between the LIDAR and optical camera. The footprint of the LIDAR is 30 m in diameter from a 20 km altitude. Once we determine the alignment from optical link experiments that were conducted from October to December 2015, we will be able to locate the footprint with an accuracy of the size.

6 Conclusion

We have reported a method to estimate the normal albedo on Ryugu from the transmitted and received pulse intensities measured by the Hayabusa2 LIDAR. For this estimation, we determined the transfer functions of the laser module and receiver, along with the utilization ratio of the laser energy with errors of 2.5%, 17.1%, and 4.2%, respectively. The error in the normal albedo due to instrument effects was found to be 18.0% at an altitude of 20 km. Future work will focus on an investigation of the LIDAR's response to the received pulses deformed by the surface slope and roughness, as well as the precise

simulation of the pulse to construct the first global normal albedo map of a C-type asteroid.

Acknowledgements We appreciate the assistance provided by the staff of the NEC corporation in conducting the verification tests of the LIDAR and providing the experimental data. We also thank Dr. Yolande for correcting the English in an early version of this paper. We wish to express our gratitude to the two anonymous reviewers. This paper was significantly improved by their kind and thorough reviews.

References

S. Abe, T. Mukai, N. Hirata, O.S. Bamouinn-Jha, A. F. Cheng, H. Demura, R. W. Gaskell, T. Hashimoto, K. Hiraoka, T. Honda, T. Kubora, M. Matsuoka, T. Mizuno, R. Nakamura, D. J. Scheeres, M. Yoshikawa, Mass and local topography measurements of Itokawa by Hayabusa, Science, 312, 1344-1347 (2006)

H. Araki, H. Noda, S. Tazawa, Y. Ishihara, S. Goossens, S. Sasaki, Lunar laser topography by LALT on board the KAGUYA lunar explorer –Operational history, new topographic data, peak height analysis of laser echo pulses, Advances in Space Research, 52, 262-271 (2013)

O.S. Barnouin-Jha, A. F. Cheng, T. Mukai, S. Abe, N. Hirata, R. Nakamura, R. W. Gaskell, J. Saito, B. E. Clark, Small-scale topography of 25143 Itokawa from the Hayabusa laser altimeter, Icarus, 198, 108-124 [2008]

R. P. Binzel, A. Morbidelli, S. Merouane, F. E. Demeo, M. Birlan, P. Vernazza, C. A. Thomas, A. S. Rivkin, S. J. Bus, A. T. Tokunaga, Earth encounters as the origin of fresh surfaces on near-Earth asteroids. Nature, 463, 331-334 (2010)

J. F. Cavanaugh, J. C. Smith, X. Sun, A. E. Bartels, L. Ramos- Izquierdo, D. J. Krebs, A. M. Novo-Gradac, J. F. McGarry, R. Trunzo, J. L. Britt, J. Karsh, R. B. Katz, A. Lukemire, R. Szymkiewicz, D. L. Berry, J. P. Swinski, G. A. Neumann, M. T. Zuber, and D. E. Smith, The Mercury Laser Altimeter instrument for the MESSENGER mission, Space Science Reviews, 131, 451-479 (2007)

B. E. Clark, J. Veverka, P. Helfenstein, P. C. Thomas, J. F. Bell Ⅲ, A. Harch, M. S. Robinson, S. L. Murchie, L. A. McFadden, C. R. Chapman, Near Photometry of Asteroid 253 Mathilde, Icarus, 140, 53-65 (1999)

E. A. Cloutis, P. Hudon, T. Hiroi, M. J. Gaffey, Spectral reflectance properties of carbonaceous chondrites: 4. Aqueously altered and thermally metamorphosed meteorites, Icarus, 220, 586-617 (2012)

A. M. Cord, P. C. Pinet, Y. Daydou, S. D. Chevrel, Planetary regolith surface analogs: optimized determination of Hapke parameters using multi-angular spectro-imaging laboratory data, Icarus, 165, 414-427 (2003)

R. Gaskell, O. Barnouin-Jha, D. Scheers, T. Mukai, N. Hirata, S. Abe, J. Saito, M. Ishiguro, T. Kubota, T. Hashimoto, J. Kawaguchi, M. Yoshikawa, K. Shirakawa, T. Kominato, Landmark-navigation studies and target characterization in the Hayabusa encounter with Itokawa, AIAA/AAS Astrodynamics Specialist Conference and Exhibit, 2006-6660, 1-12 (2006)

N. Hirata and M. Ishiguro, Properties and possible origin of black boulders on the asteroid Itokawa: in abstract of 42nd Lunar and Planetary Science Conference (2011)

M. Ishiguro, D. Kuroda, S. Hasegawa et al., Optical properties of (162173) 1999JU3: In preparation for the JAXA Hayabusa2 sample return mission, The Astrophysical Journal, 792, 1-9 (2014)

B. Lohani, N. Bhatnager, A. Roshan, Return pulse waveform simulation for LLRI instrument onboard Chandrayan- Ⅰ, Journal of the Indian Society of Remote Sensing, 36, 1, 1-11 (2008)

P. G. Lucey, G. A. Neumann, M. A. Riner, E. Mazarico, D. E. Smith, M. T. Zuber, D. A. Paige, D. B. Bussey, J. T. Cahill. A. McGovern, P. Isaacson, L. M. Corely, M. H. Torrence, H. J. Melosh, J. W. Head, E. Song, The global albedo of the Moon at 1064 nm, Journal of Geophysical Research Planets, 119, 1665 (2014)

M. Matsuoka, T. Nakamura, Y. Kimura, T. Hiroi, R. Nakamura, S. Okumura, S. Sasaki, Pulse-laser irradiation experiments of Murchison CM2 chondrite for reproducing space weathering on C-type asteroids, Icarus, 254, 135-143 (2015)

T. Mizuno, T. Kase, T. Shiina, M. Mita, N. Namiki, H. Senshu, R. Yamada, H. Noda, H. Kunimori, N. Hirata, F. Terui, Y. Mimasu, Development of the laser altimeter (LIDAR) for Hayabusa2, Space Science Reviews, this issue (2016)

N. A. Moskovitz, S. Abe, K. Pan, D. J. Osip, D. Pefkou, M. D. Melita, M. Elias, K. Kitazato, S. J. Bus, F. E.. Demeo, R. P. Binzel, P. A. Abell, Rotational characterization of Hayabusa Ⅱ target asteroid (162173) 1999 JU3, Icarus, 224, 24-31 (2013)

T. Mukai, S. Abe, N. Hirata, R. Nakamura, O. S. Barnouin-Jha, A. F. Cheng, T. Mizuno, K. Hiraoka, T. Honda, H. Demura, R. W. Gaskell, T. Hashimoto, T. Kubota, M. Matsuoka, D. J. Scheeres, M. Yoshikawa, An overview of the LIDAR observations of asteroid 25143 Itokawa, Advances in Space Research, 40, 187-192 (2007)

N. Namiki, T. Mizuno, N. Hirata, H. Noda, H. Senshu, R. Yamada, H. Ikeda, S. Abe, K. Matsumoto, S. Oshigami, M. Shizugami, F. Yoshida, N. Hirata, H. Miyamoto, S. Sasaki, H. Araki, S. Tazawa, Y. Ishihara, M. Kobayashi, K. Wada, H. Demura, J. Kimura, M. Hayakawa, N. Kobayashi, Scientific use of LIDAR data of Hayabusa-2 mission, Proceeding of an International CJMT-1 Workshop on Asteroidal Science, 74-96 (2014)

G. A. Neumann, J. F. Cavanaugh, X. Sun, E. Mazarico, D. E. Smith, M. T. Zuber, D. Mao, D. A. Paige, S. C. Solomon, C. M. Ernst, O.S. Barnouin, Bright and dark polar deposits on Mercury: Evidence for surface volatiles, Science, 339, 296-300 (2013)

V. Reddy, A. Nathues, L. Corre et al., Color and albedo heterogeneity of Vesta from Dawn, Science, 336, 700-703 (2012)

M. R. Santovito, L. Tommasi, G. Sgarzi, A. Romoli, S. Matteri, E. Murphy, N. Rando, A laser altimeter for BepiColombo mission: Instrument design and performance model, Planetary and Space Science, 54, 645-660 (2006)

J. Saito, H. Miyamoto, R. Nakamura, M. Ishiguro, T. Michikami, A. M. Nakamura, H. Demura, S. Sasaki, N. Hirata, C. Honda, A. Yamamoto, Y. Yokota, T. Fuse, F. Yoshida, D. J. Tholen, R. W. Gaskell, T. Hashimoto, T. Kubota, Y. Higuchi, E. Nemoto, A. Yukishita, K. Kitazato, B. Dermawan, A. Sogame, J. Terazono, C. Shinohara, H. Akiyama, Detailed images of asteroid 25143 Itokawa from Hayabusa, Science, 312, 2, 1341-1344 (2006)

D. E. Smith, M. T. Zuber, G. B. Jackson, G. A. Neumann, H. Riris, X. Sun, R. S. Zellar, C. Coltharp, J. Connelly, R. B. Katz, I. Kleyner, P. Liiva, A. Matuszeski, E. M. Mazarico, J. F. McGarry, A.-M. Novo-Gradac, M. N. Ott, C. Peters, L. A. Ramos-Izquierdo, L. Ramsey, D. D. Rowlands, S. Schmidt, V. S. Scott III, G. B. Shaw, J. C. Smith, J.-P. Swinski, M. H. Torrence, G. Unger, A. W. Yu, T. W. Zagwodzki, The Lunar Orbiter Laser Altimeter Investigation on the Lunar Reconnaissance Orbiter Mission, Space Science Reviews, 150, 209-241 (2010)

S. Sugita, D. Kuroda, S. Kameda, S. Hasegawa, S. Kamata, M. Abe, M. Ishiguro, N. Takato, M. Yoshikawa, Visible spectroscopic observation of asterioid 162173 (1999ju3) with the Gemini-s telescope, In: 44th DPS Meeting. American Astronomical Society (Abstract 102.02) (2013)

X. Sun et al., Calibration of the Mercury Laser Altimeter on the MESSENGER spacecraft, IEEE

Transactions on Geoscience and Remote Sensing, 53, 5, 2860-2874 (2015)

E. F. Tedesco, IRAS Minor Planet Survey (IMPS), Phillips Laboratory, Technical Report PL-TR-92-2049. Hanscom Air Force Base, MA, (1992).

J. Veverka, P. C. Thomas, A. Harch, B. E. Clark, J. Bell, B. Carcich, J. Joseph, C. R. Chapman, W. Merline, M. S. Robinson, M. Malin, L. A. McFadden, S. L. Murchie, R. Farquhar, N. R. Izenberg, A. Cheng, NEAR's flyby of 253 Mathilde: Images of a C asteroid, Science, 278, 2109-2113 (1997)

F. Vilas, Spectral characteristics of Hayabusa2 near-earth asteroid targets 162173 1999JU3 and 2001 QC34, The Astronomical Journal, 135, 1101-1105 (2008)

M. T. Zuber, J. W. Head, D. E. Smith, G. A. Neumann, E. Mazarico, M. H. Torrence, O. Aharonson, A. R. Tye, C. Fassert, M. A. Rosenburg, H. J. Melosh, Constraints on the volatile distribution within Shackleton crater at the lunar south pole, Nature, 486, 378-382 (2012)